

Semi-Dirac Fermions in a Topological Metal

Yinming Shao^{1,*}, Seonghill Moon^{2,3}, A. N. Rudenko⁴, Jie Wang^{5,6,7}, Mykhaylo Ozerov³, David Graf³, Zhiyuan Sun⁶, Raquel Queiroz¹, Seng Huat Lee⁸, Yanglin Zhu⁸, Zhiqiang Mao⁸, M. I. Katsnelson⁴, Dmitry Smirnov³, Andrew. J. Millis^{1,9}, D. N. Basov¹

¹Department of Physics, Columbia University, New York, NY, 10027, USA

²Department of Physics, Florida State University, Tallahassee, FL, 32306, USA

³National High Magnetic Field Laboratory, Tallahassee, FL, 32310, USA

⁴Institute for Molecules and Materials, Radboud University, Nijmegen, The Netherlands

⁵Center of Mathematical Sciences and Applications, Harvard University, Cambridge, MA, 02138, USA

⁶Department of Physics, Harvard University, Cambridge, MA, 02138, USA

⁷Department of Physics, Temple University, Philadelphia, Pennsylvania, 19122, USA.

⁸Department of Physics, Pennsylvania State University, University Park, PA, 16802, USA

⁹Center for Computational Quantum Physics (CCQ), Flatiron Institute, New York, NY, 10010, USA

Abstract

Topological semimetals with massless Dirac and Weyl fermions^{1,2} represent the forefront of quantum materials research. In two dimensions (2D), a peculiar class of fermions that are massless in one direction and massive in the perpendicular direction was predicted fifteen years ago^{3–5}. These highly exotic quasiparticles – the semi-Dirac fermions – ignited intense theoretical interest^{6–14} but remain undetected. Using magneto-optical spectroscopy, we demonstrate the defining feature of semi-Dirac fermions – $B^{2/3}$ scaling of Landau levels – in a prototypical nodal-line metal ZrSiS^{15,16}. In topological metals, including ZrSiS, nodal-lines extend the band degeneracies from isolated points to lines, loops^{17,18} or even chains^{19–22} in the momentum space. With *ab initio* calculations and theoretical modeling, we pinpoint the observed semi-Dirac spectrum to the crossing points of nodal-lines in ZrSiS. Crossing nodal-lines exhibit a continuum absorption spectrum but with singularities that scale as $B^{2/3}$ at the crossing. Our work sheds light on the hidden quasiparticles emerging from the intricate topology of crossing nodal-lines^{19,23}.

Main text

Conventional 2D fermions are described by parabolic energy (E)-momentum (k) dispersion $E(\mathbf{k}) = \hbar^2 k^2 / (2m)$ with effective mass m . In contrast, Dirac fermions have linear dispersion $E_D(\mathbf{k}) = \hbar v_F k$ and are massless. The striking manifestations of massless Dirac fermions are revealed through the anomalous half-integer quantum Hall effect^{24,25}, Klein tunneling^{26,27}, and \sqrt{B} scaling of Landau levels (LLs) with magnetic fields (B)^{28–30} in graphene. All these effects are observed in graphene, with the characteristic \sqrt{B} scaling provides a litmus test for Dirac quasiparticles.

Semi-Dirac fermions, with dispersion $E_{SD}(\mathbf{k}) = \hbar v k_1 + \hbar^2 k_2^2/(2m)$ being linear in one momentum direction and quadratic in the orthogonal direction, have been proposed to appear in materials where multiple Dirac points merge^{3,9} into a semi-Dirac point. Strained graphene may be a candidate system to host semi-Dirac quasiparticles. However, the required uniaxial strain level is unrealistically large^{3,31,32}. Black phosphorus (BP) is proposed as another candidate semi-Dirac fermions system upon strong doping³³. Yet the precise semi-Dirac dispersion in BP has not been established either experimentally³⁴ or theoretically³⁵. Thus far, the semi-Dirac dispersion E_{SD} has been experimentally explored only in synthetic platforms including honeycomb lattices of ultracold atoms³⁶ and photonic resonators^{37–39}. Identifying the fermionic counterpart is crucial to realize the diverse topological^{9,10} and correlated^{11,40} phases predicted for semi-Dirac fermions, but remains challenging in 2D systems. A defining feature of semi-Dirac fermions is the unique $B^{2/3}$ dependence^{3,5} of inter-LL transitions (Fig. 1a). Here we report on the first observation of this characteristic $B^{2/3}$ power-law in a topological metal, ZrSiS, through LL spectroscopy.

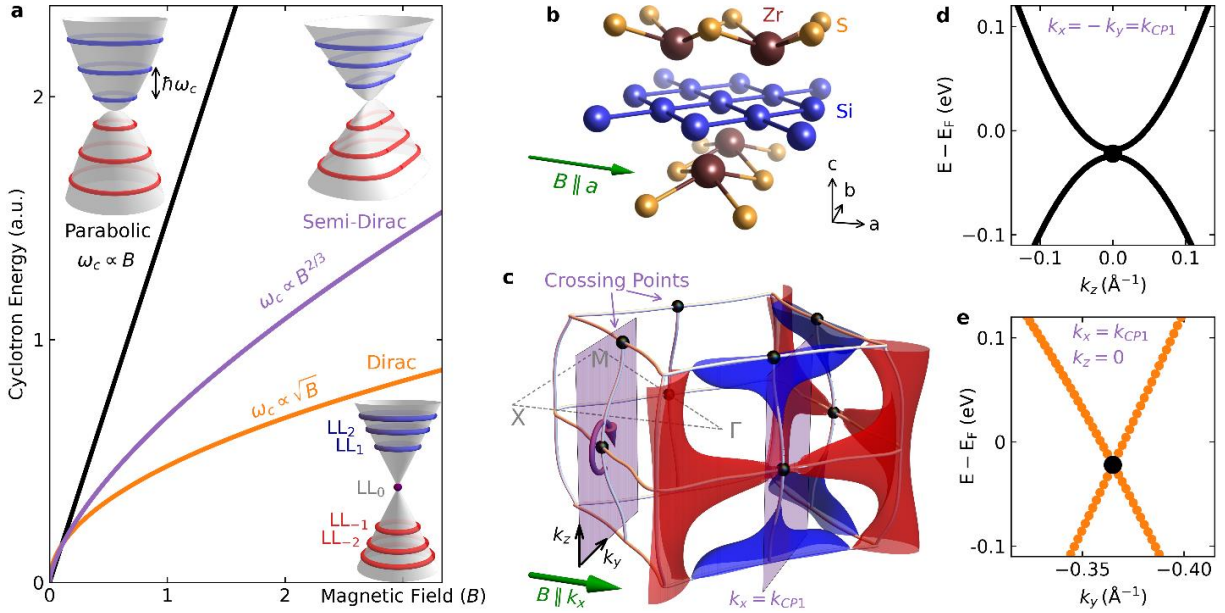


Fig. 1| Semi-Dirac fermions at nodal-line crossing points in ZrSiS. **a**, Cyclotron energy ($\hbar\omega_c$) as a function of magnetic field (B) for conventional fermions (black), Dirac fermions (orange), and semi-Dirac fermions (purple). Insets show three dimensional plots of their band structures (grey surfaces) overlaid with Landau levels (red and blue contour lines). **b**, The lattice structure of ZrSiS, showing the square lattice of Si atoms (blue) and the Zr (brown)-S (yellow) layers above and below. **c**, *ab-initio* calculation of the Fermi surface and nodal-line structure of ZrSiS. Only the $k_x > 0$ part of the Fermi surface is shown for better visualization of the nodal-line structures (gray). Black spheres indicate the crossing points (CPs) of multiple nodal-lines. Purple shaded planes at $k_x = \pm k_{CP1} = \pm 0.1971$ ($2\pi/a$) cross the CP1 formed by nodal-lines at $k_z = 0$ and $k_x = \pm k_y$. The circular purple arrow illustrates the cyclotron motion around one of the CP1 for magnetic field (green arrow) applied along k_x (a -axis of the crystal). Calculated band structure (see Methods and Supplementary Information Sec. III) near CP1 at $k_x = k_{CP1}$ plane shows quadratic dispersion (**d**) and linear dispersion (**e**) along k_z and k_y , characteristic of semi-Dirac fermions.

Semi-classically, a magnetic field induces cyclotron motion and the area of the cyclotron orbit at energy E is $S(E) \propto E^{3/2}\sqrt{m}/v$ for the semi-Dirac dispersion E_{SD} ³. Following the Onsager

quantization⁴¹ $S(E) = 2\pi(n + \gamma)eB/\hbar$, the characteristic $B^{2/3}$ scaling of LLs is obtained: $E_n \propto [(n + \gamma)B]^{2/3}$, where n is the LL index and γ is the phase factor ($0 \leq \gamma < 1$). The 2D semi-Dirac spectrum can also arise as singularity points of a continuum absorption spectrum of a 3D material. For example, the LL spectrum of a nodal-ring ($E_{NR} = \pm \sqrt{\left(\frac{k_x^2 + k_y^2 - k_0^2}{2m}\right)^2 + v_z^2 k_z^2}$) with field in the $x - y$ plane exhibits a continuum absorption with a lower edge scaling as $B^{2/3}$, arising from the semi-Dirac structure (see Methods).

The prototypical nodal-line semimetal ZrSiS^{15,16,42} (Fig. 1b) hosts two planar nodal-squares linked by vertical nodal-lines, forming a chain-like structure^{19,20} (gray lines in Fig. 1c) in momentum space. The low-energy physics of the ZrSiS family of nodal metals is further enriched by the Fermi energy variations along the Dirac nodal-lines^{43–45}, reflected by the coexisting electron (blue) and hole (red) pockets (Fig. 1c). *Ab initio* calculations and theoretical modeling show that the observed semi-Dirac fermions originate from the crossing points (CPs) of the nodal-lines in ZrSiS (black dots in Fig. 1c). Near the CP, the band structure at $k_x = k_{CP}$ shows quadratic (Fig. 1d) and linear (Fig. 1e) dispersion along k_z and k_y , respectively. Under magnetic field oriented along a-axis (i.e. $B \parallel k_x$), the cyclotron motion of electrons becomes quantized in the (k_y, k_z) plane and reflects the semi-Dirac fermions through the unique LL scaling. We find that the anticipated $B^{2/3}$ power-law in ZrSiS is robust against material complexities and can be readily identified in infrared magneto-optics experiments.

We now proceed to the magneto-reflectance spectra $R(\omega, B)$ normalized by the zero-field data $R(\omega, 0 \text{ T})$ for ZrSiS with in-plane magnetic fields up to 17.5 T (see Methods), shown in Fig. 2a. The most prominent features are a series of dips in the reflectance spectra hardening with increasing field (gray dashed lines). For a highly metallic system like ZrSiS, the infrared reflectance approaches unity and therefore dips in $R(B)/R(0)$ correspond to absorption $A(\omega) = 1 - R(\omega)$ ^{43,45}. We attributed these absorption features to interband LL transitions from massive Dirac fermions ($E_{\pm n} = \sqrt{2e\hbar|n|B\bar{v}^2 + \Delta^2}$), which exhibit notable departures from the linear-in- B scaling expected for fermions in parabolic bands (Fig. 1a). Here, Δ is half of the spin-orbit-coupling (SOC) gap^{45–48} and we find $2\Delta \approx 28 \text{ meV}$, in excellent agreement with previous lower-field studies^{43,49} and calculations¹⁵. Surprisingly, above a critical field $B_c \approx 7 \text{ T}$, weaker sub-gap features (red and purple dots) appear at around 100 cm^{-1} and harden with increasing field. To better visualize these sub-gap structures, we report the second derivative d^2R/dB^2 analysis in Fig. 2b. The local minima of the second derivative coincide with the dips in $R(B)/R(0)$ (see Supplementary Information Sec. I), which we identify as the LL transition energies in all analyses.

In Fig. 2b, we show the d^2R/dB^2 spectra for ZrSiS obtained with in-plane magnetic fields up to 17.5 T. The gray dashed lines denote the model calculation of interband LL transitions across the gapped Dirac cone⁴⁶: $E_T = \sqrt{2e\hbar|n|B\bar{v}^2 + \Delta^2} + \sqrt{2e\hbar(|n| + 1)B\bar{v}^2 + \Delta^2}$, where n is the LL index and \bar{v} is the averaged Fermi velocity. The intraband LL transitions⁵⁰, if present, would follow a field dependence distinct from the observed sub-gap features (see Extended Data Fig. 3 and Extended Data Fig. 4). Importantly, beyond the two series of sub-gap transitions labeled as

\sqrt{B} and $B^{2/3}$ (red and purple dots, respectively), two additional dispersive features are apparent above 150 cm^{-1} . As indicated by the thick orange lines, the dispersions of these latter features also follow approximately the \sqrt{B} scaling.

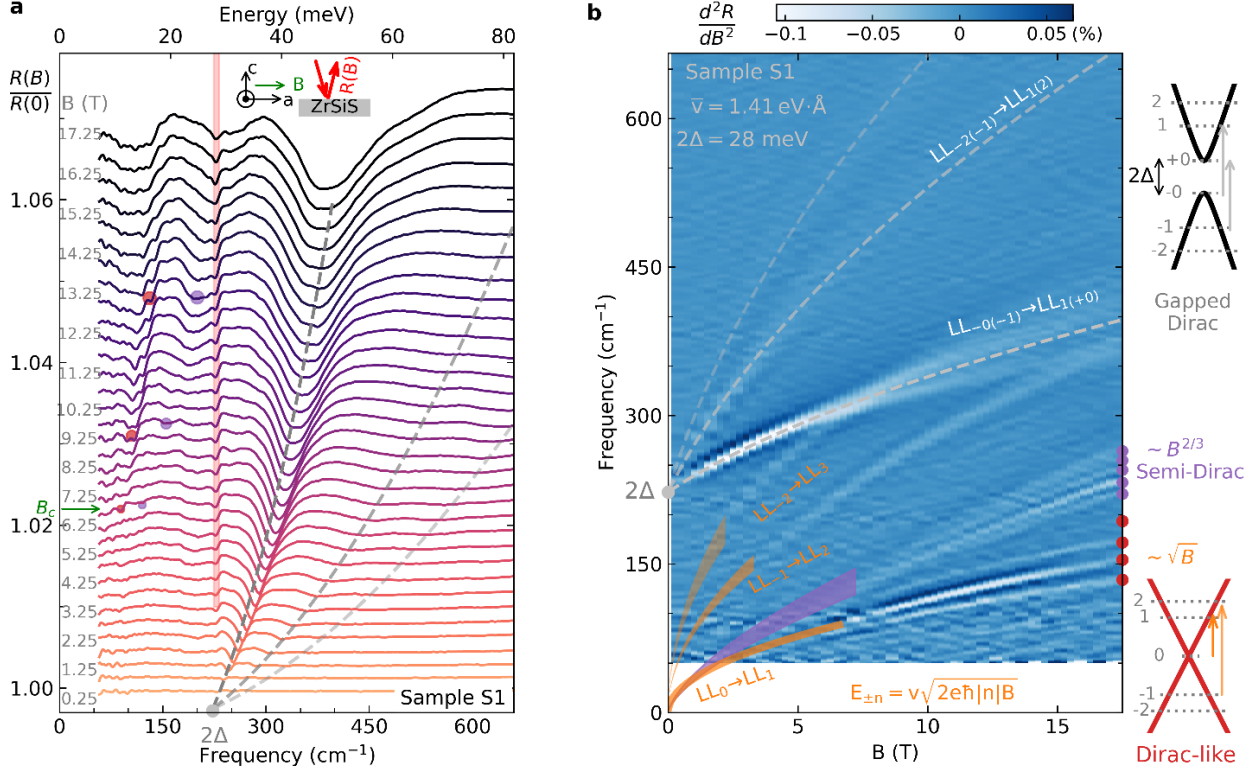


Fig. 2|Landau-level spectroscopy of ZrSiS with in-plane magnetic fields. a, Magneto-reflectance $R(\omega, B)$ normalized by zero-field reflectance $R(\omega, 0 \text{ T})$ for sample S1. Gray dashed lines mark the positions of the series of interband LL transitions across the spin-orbit coupling gap ($2\Delta \approx 28 \text{ meV}$). The red-shaded region indicates a potential phonon feature that is not dispersing with increasing field. Above a critical field of $B_c \approx 7 \text{ T}$, additional sub-gap transitions (red and purple dots) emerge and harden with increasing field. Inset is a schematic of the experimental configuration with near-normal incident and unpolarized light while the magnetic field is applied in-plane ($B \perp c, B \parallel a$, Voigt geometry). **b,** Second derivative d^2R/dB^2 data of sample S1 overlaid with model fitting (gray dashed lines) of the LL transitions across the gapped Dirac cone. The top schematic shows a gapped Dirac cone with gap 2Δ and the first LL transitions $LL_{-0(-1)} \rightarrow LL_{1(+0)}$ (gray arrows). Orange lines are the guides for the sub-gap LL transitions (red dots in **a**) that follow approximately \sqrt{B} scaling, characteristic of a Dirac-like fermion (bottom schematic). The sub-gap features near the purple-shaded region follow a distinct $B^{2/3}$ power-law and originate from semi-Dirac fermions.

The dipole selection rule $\delta|n| = \pm 1$ ^{28,30} for Dirac fermions dictates that the energy ratios of the lowest three interband LL transitions are: $1: 1 + \sqrt{2}: \sqrt{2} + \sqrt{3}$. Using a single averaged velocity of $0.82 \text{ eV}\text{\AA}$, the three branches of the transitions can be approximated by the lowest three interband LL transitions from massless Dirac-like fermions (orange lines) and are labeled $LL_{0 \rightarrow 1}$, $LL_{-1 \rightarrow 2}$ and $LL_{-2 \rightarrow 3}$. Detailed analysis on the multiple peak splitting of $LL_{0 \rightarrow 1}$ below shows evidence of a small gap and spin-splitting due to Zeeman effect. On the other hand, the

remaining sub-gap features (near purple shaded region in Fig. 2b) follow sub-linear B -dependence that is distinct from \sqrt{B} . We will confirm next that these peculiar LL transitions' field dependence scales precisely as $B^{2/3}$, a fingerprint of semi-Dirac fermions in ZrSiS.

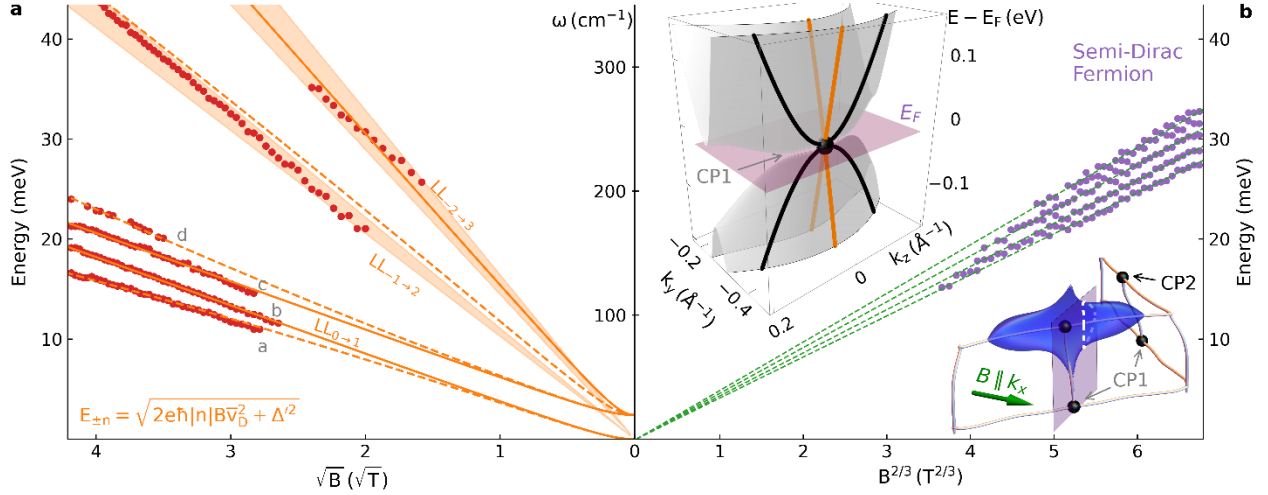


Fig. 3 | \sqrt{B} and $B^{2/3}$ power-law behaviors of Landau levels in ZrSiS. **a**, Sub-gap transition energies (red dots) in Fig. 2 are plotted as a function of \sqrt{B} . Orange lines represent the fitting based on Dirac-like fermions with an averaged Fermi velocity $\bar{v}_D = 0.88 \text{ eV\AA}$, a small gap $2\Delta' = 2.4 \text{ meV}$, and Zeeman g-factor $g = 2.6$. Solid and dashed lines represent the spin-conserving and spin-flip transition, respectively. Orange shaded areas indicate the uncertainties in \bar{v}_D for the $LL_{-1 \rightarrow 2}$ ($\bar{v}_D^{-1 \rightarrow 2} = (0.91 \pm 0.04)\bar{v}_D$) and $LL_{-2 \rightarrow 3}$ ($\bar{v}_D^{-2 \rightarrow 3} = (1.02 \pm 0.07)\bar{v}_D$) transitions. **b**, Higher-energy sub-gap transitions in Fig. 2 (purple dots) are plotted as a function of $B^{2/3}$, following the exact power-law behavior expected for semi-Dirac fermions (green dashed lines). The bottom inset shows the calculated Fermi surface of ZrSiS. The shaded purple plane indicates the $k_x = k_{CP1}$ plane, which cuts through CP1 (black dot at $k_z = 0$). The top inset shows the calculated band structure E vs. k_y, k_z for CP1 at the plane $k_x = k_{CP1}$, with linear dispersion along k_y and quadratic dispersion along k_z , characteristic of semi-Dirac dispersion.

To quantify the power-law scaling of the sub-gap features, we extract the transition energies from Fig. 2b (see Extended Data Fig. 3) and plot them against \sqrt{B} and $B^{2/3}$ in Fig. 3a and Fig. 3b, respectively. Fig. 3a shows the experimentally determined LL transition energies (red dots) for the three groups of transitions labelled $LL_{0 \rightarrow 1}$, $LL_{-1 \rightarrow 2}$, $LL_{-2 \rightarrow 3}$ in Fig. 2b. Remarkably, all these LL transitions can be understood as originating from a Dirac fermion with a small gap $2\Delta' = 2.4 \text{ meV}$ and Zeeman-split LLs. The resulting model calculations (orange lines) show good agreement with the data (see Extended Data Fig. 5 for details). For $LL_{-2 \rightarrow 3}$, variation of \bar{v}_D shows a logarithmic reduction with increasing B field ($\bar{v}_D \propto -\ln(B)$, see Extended Data Fig. 6b). Alternatively, the $LL_{-1 \rightarrow 2}$ and $LL_{-2 \rightarrow 3}$ transitions can arise from the cyclotron resonance associated with another gapped Dirac cone⁵⁰ (Extended Data Fig. 6a) and the exact origin of these two transitions awaits future studies.

As we alluded previously, a series of sub-gap features displays the $B^{2/3}$ scaling that is characteristic of semi-Dirac fermions (Fig. 3b). Fine splitting of LL transitions is also apparent and all the split peaks agree with the predicted power-law behavior (green dashed lines) for

semi-Dirac fermions. These latter features are reminiscent of the spin and valley splitting of Landau levels in Dirac fermions^{51,52} and we discuss several possible scenarios for peak splitting in the Supplementary Information Sec. II and Figs. S3-S6.

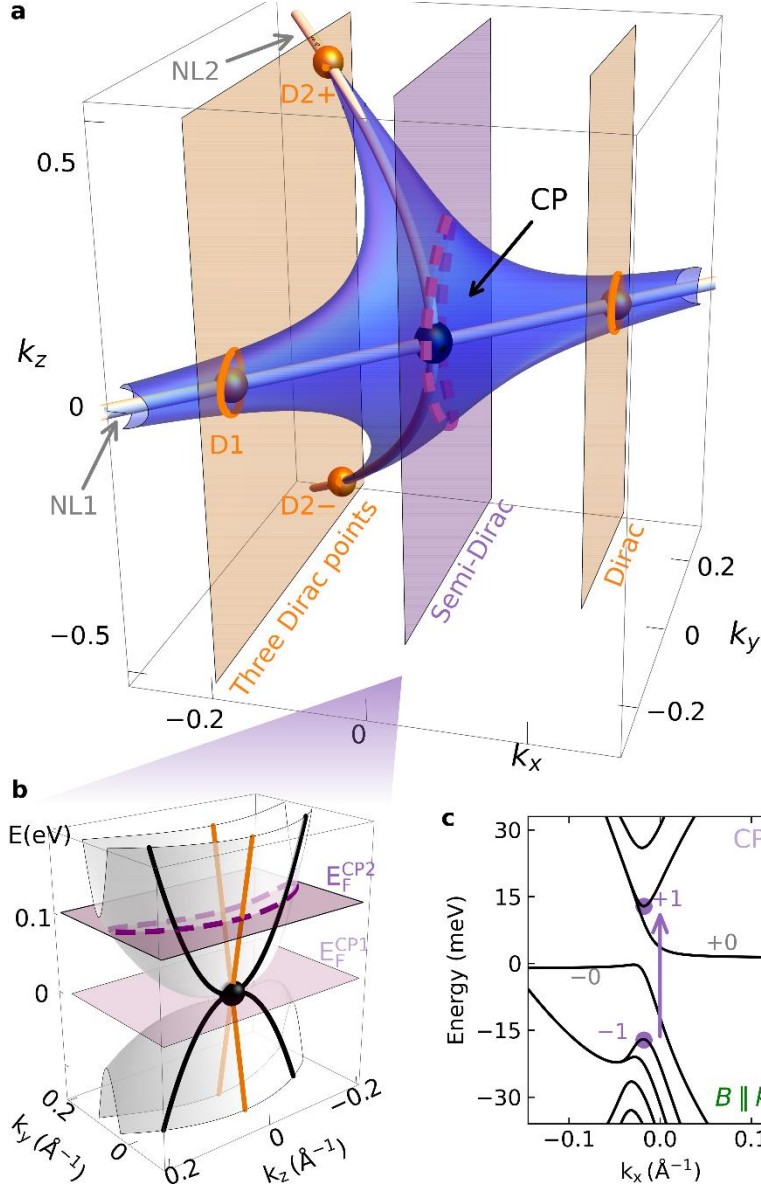


Fig. 4| Model for the crossing point of two nodal lines. **a**, Fermi surface (blue) of the two-band model Eq. (1). The orange shaded plane at $k_x = -0.2$ crosses the nodal line NL1 at $\mathbf{k}_{D1} = (k_x, k_x, 0)$ and crosses NL2 at $\mathbf{k}_{D2\pm} = (k_x, -k_x, \pm\sqrt{4mv|k_x|})$. Purple shaded plane at $k_x = 0$ cuts through the CP (black sphere) of NL1 and NL2 at the origin $\mathbf{k} = (0, 0, 0)$. **b**, Band structure E vs. k_y, k_z at $k_x = 0$, showing a semi-Dirac point (black sphere) as a result of the merging of three Dirac points at \mathbf{k}_{D1} and $\mathbf{k}_{D2\pm}$. Purple dashed lines in **a** and **b** show the crescent-shaped Fermi surface contour of semi-Dirac fermions. Purple shaded planes represent the Fermi level for CP1 ($E_F^{CP1} \approx 0$) and CP2 ($E_F^{CP1} \approx 0.1$ eV). **c**, Calculated LL spectrum based on model parameters for CP1 at $B = 17.5$ T. Purple dots label the extremal points in the LLs and purple arrow indicate the lowest momentum-conserving transition (LL_{-1→+1}), see Extended Data Fig. 8 and Supplementary Information Sec. IV for details.

Importantly, the semi-Dirac fermions in ZrSiS are confirmed both from *ab initio* calculations and from theoretical modeling of the crossing points (CPs) of nodal-lines. As shown in the bottom inset of Fig. 3b, there are two non-equivalent CPs in ZrSiS, labeled as CP1 (at $k_z = 0$) and CP2 (at $k_z = \pi/c$). The observed $B^{2/3}$ scaling LL transition is dominated by CP1 since the energy of the CP is very close to the Fermi level, while the energy of CP2 is about 0.1 eV below the Fermi level (Fig. S9). The calculated semi-Dirac bands near the CP1 (Fig. 3b top inset) is also asymmetric in k_y , in contrast to the usual semi-Dirac dispersion³: $E_{SD} = \sqrt{k_y^4/4m^2 + v^2k_z^2}$. We demonstrate below that a unique semi-Dirac fermion that originates from the merging of three Dirac points⁹ is realized near CP1 in ZrSiS, distinct from the merging of two Dirac points^{3,6} realized in a single nodal-ring (Supplementary Video 1).

We now turn to the theoretical interpretation of the results. In contrast to the intersection of two straight nodal-lines²⁰ or two nodal-rings²³, the CP1 in ZrSiS is comprised of a straight nodal-line and a curved nodal-line (see Fig. 1c and Extended Data Fig. 1), which can be described by a minimum two-band model for the CP:

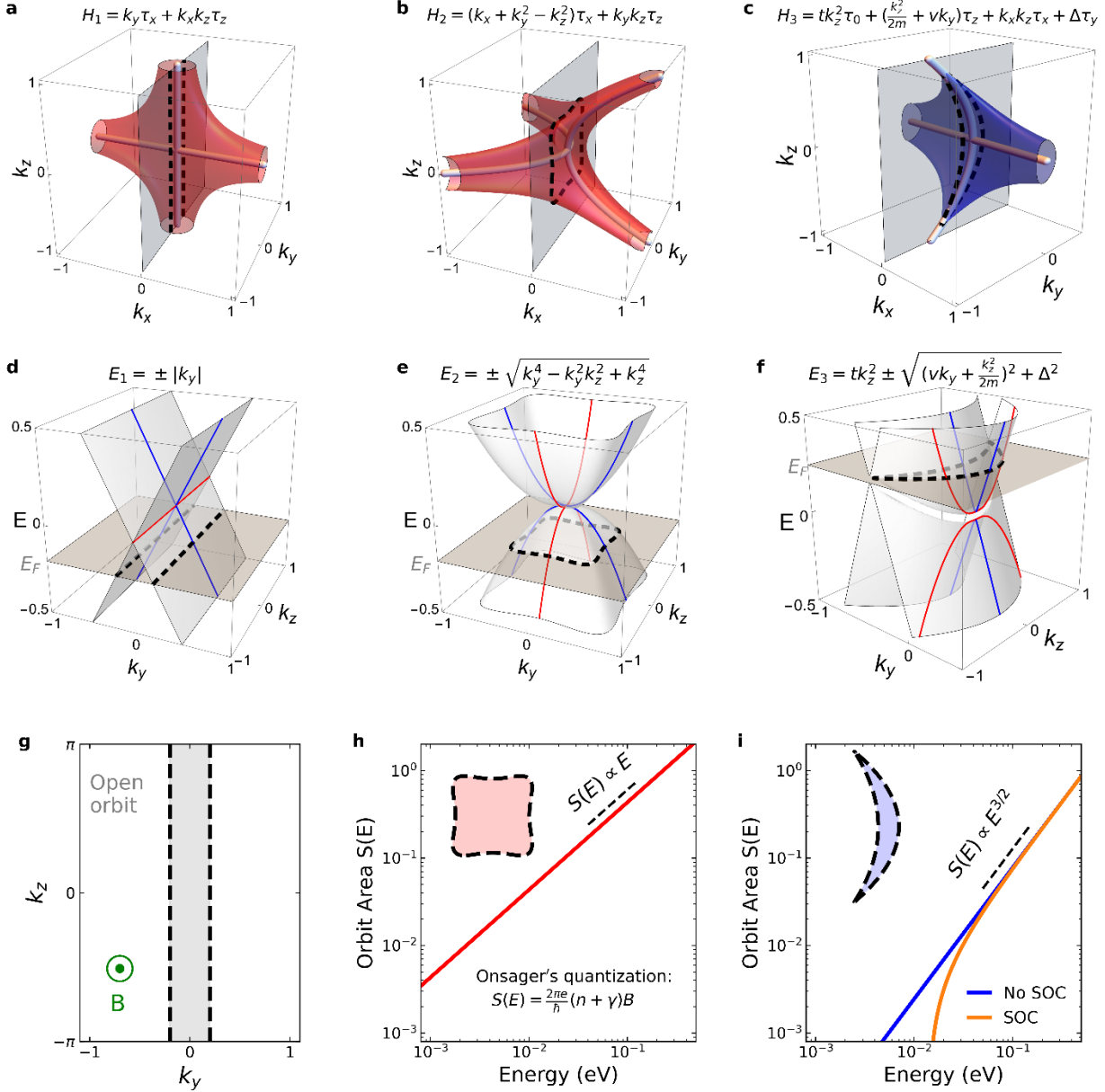
$$H_{CP} = t_1 k_z^2 \tau_0 + \left(\frac{k_z^2}{2m} + vk_{\perp} \right) \tau_z + t_2 k_{\parallel} k_z \tau_x + \Delta' \tau_y \quad (1)$$

where τ_0 is the identity matrix, τ_i ($i = x, y, z$) are the Pauli matrices, m is the effective mass along the k_z direction, v is the Fermi velocity along $k_{\perp} = k_x - k_y$ direction, t_1 controls the electron-hole asymmetry (tilt of the nodal-line along z), t_2 controls the dispersion along $k_{\parallel} = k_x + k_y$ (parallel to the in-plane nodal-line), and Δ' is half of the SOC gap. As shown in Fig. 4a, the spectrum of Eq. (1) describes the crossing of a straight in-plane nodal-line (NL1, bounded by the $k_z = 0$ and $k_x = k_y$ planes) and a curved vertical nodal-line (NL2, bounded by the $k_x = -k_y$ and $k_y = \frac{k_z^2}{4mv}$ planes). The Fermi surface (FS) of the model (Fig. 4a) captures the main features of the FS in ZrSiS near the CP2 (Fig. 3b bottom inset). In particular, the crescent-shape FS contour at the CP (purple dashed line) is consistent with band structure calculations of ZrSiS and further corroborated with quantum oscillation measurements (Extended Data Fig. 7). Under the external magnetic field along x , the 2D plane normal to the field at negative k_x will cross NL1 once and cross NL2 twice, forming three isolated Dirac points (D1 and D2 \pm). As the 2D plane moves to the right, the three Dirac points get closer and merge at $k_x = 0$ (purple shaded plane), realizing a type-II semi-Dirac fermion⁹: $H'_{SD} = t_1 k_z^2 \tau_0 + (\frac{k_z^2}{2m} - vk_y) \tau_z + t_2 k_y k_z \tau_x$ (Fig. 4b). At $k_x > 0$ the spectrum becomes a single Dirac again. The unique semi-Dirac fermion described by H'_{SD} are predicted to exhibit nontrivial Berry phase and finite Chern number when a gap opens⁹. This is in stark contrast with the zero Berry phase for semi-Dirac fermions formed by merging an even number of Dirac points ($\pi \times 2n \text{ modulo } 2\pi = 0$). Crossing nodal-lines described by Eq. (1) therefore offer a new platform for studying the rich phenomena of merging Dirac points^{36,53} (see Supplementary Video 2), where topology and correlation effects intertwine.

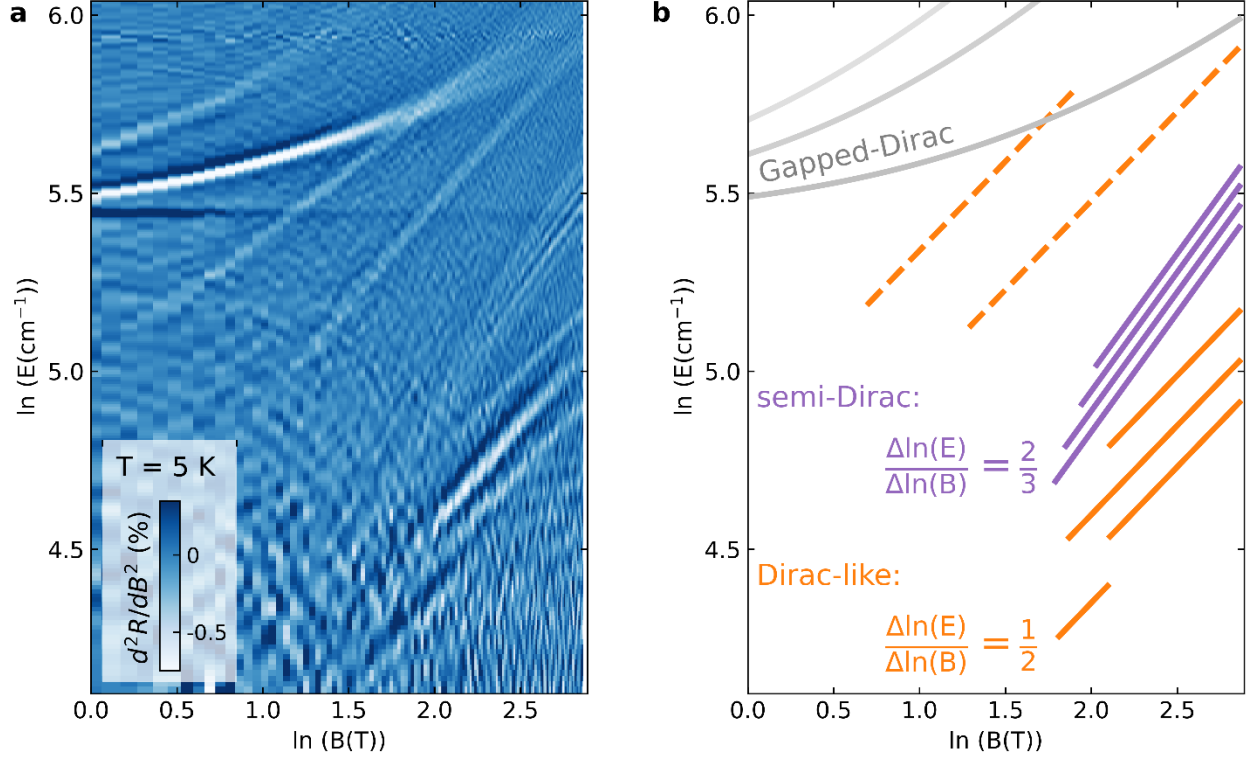
We have calculated the Landau level spectrum of Eq. (1) in the presence of an in-plane field directed along x as a function of k_x , and the results are shown in Fig. 4c. Since k_x is a good quantum number for $B \parallel k_x$, at each k_x the LL spectrum is a series of discrete levels, with level

spacing determined by the projection of the constant energy contours onto the plane perpendicular to k_x . The LLs exhibit extremal points near $k_x = 0$, as indicated by purple dots in Fig. 4c. Optical transitions (vertical purple arrow) between these LL singularities are observed experimentally in LL spectroscopy. We further demonstrate the $B^{2/3}$ scaling of the LLs at the CP using both semi-classical quantization (see Methods and Extended Data Fig. 1i) and full LL calculation with SOC (Extended Data Fig. 8 and Supplementary Information Sec. IV.).

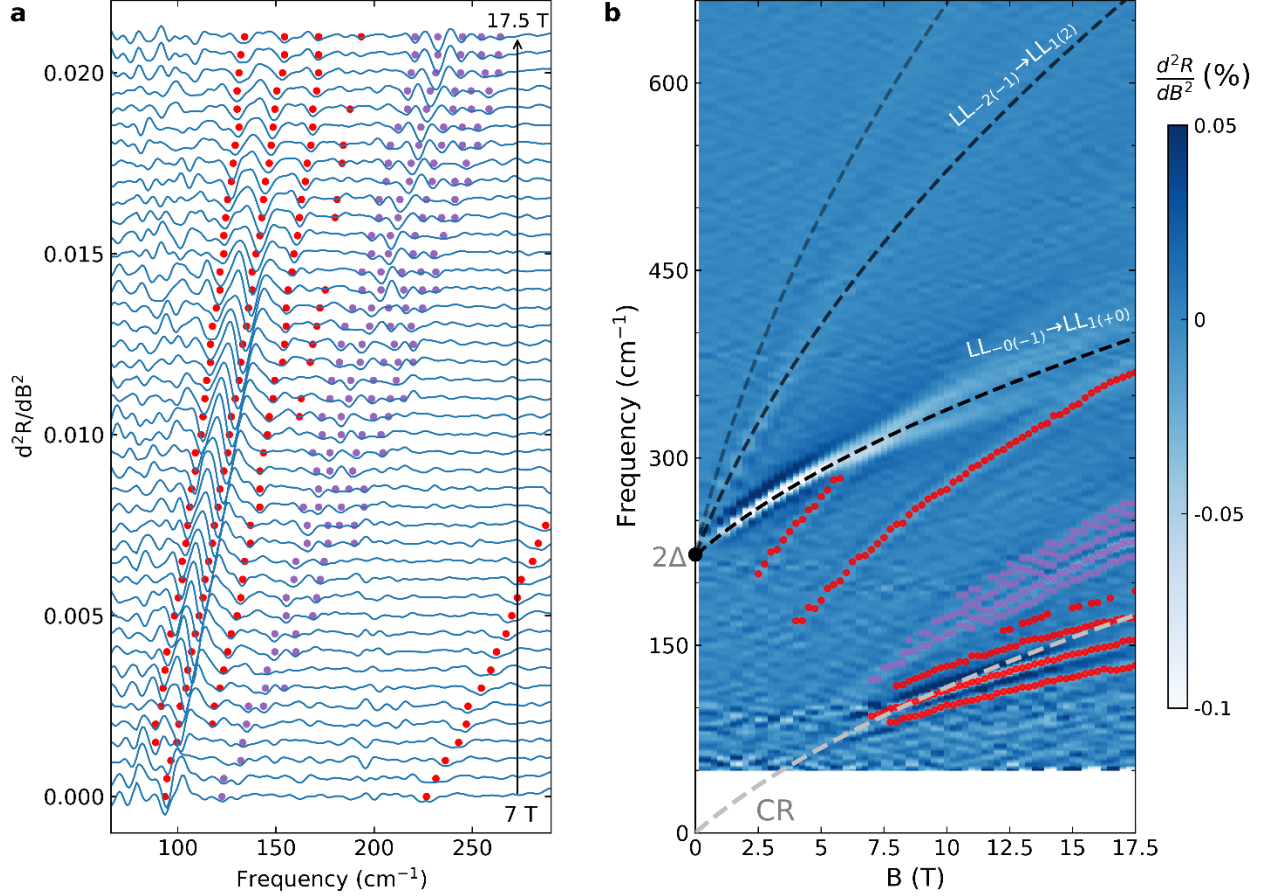
Using Landau-level spectroscopy, we uncovered semi-Dirac fermions inside bulk ZrSiS under in-plane magnetic fields. In contrast to the conventional expectation of 2D electrons at the surface/interface of a layered material, the observed semi-Dirac fermions reside within planes perpendicular to the atomic layers of ZrSiS and originate from the vicinity of points where nodal-lines cross. The crossing point of nodal-lines in ZrSiS offers a unique and generic platform for realizing semi-Dirac fermions through the merging of three Dirac points. Our findings advance the understanding of exotic 2D electrons in natural bulk crystals, establish the existence of novel quasiparticles associated with crossing nodal lines in momentum space^{19,23}, and open new directions in understanding correlation and topological effects in metals.



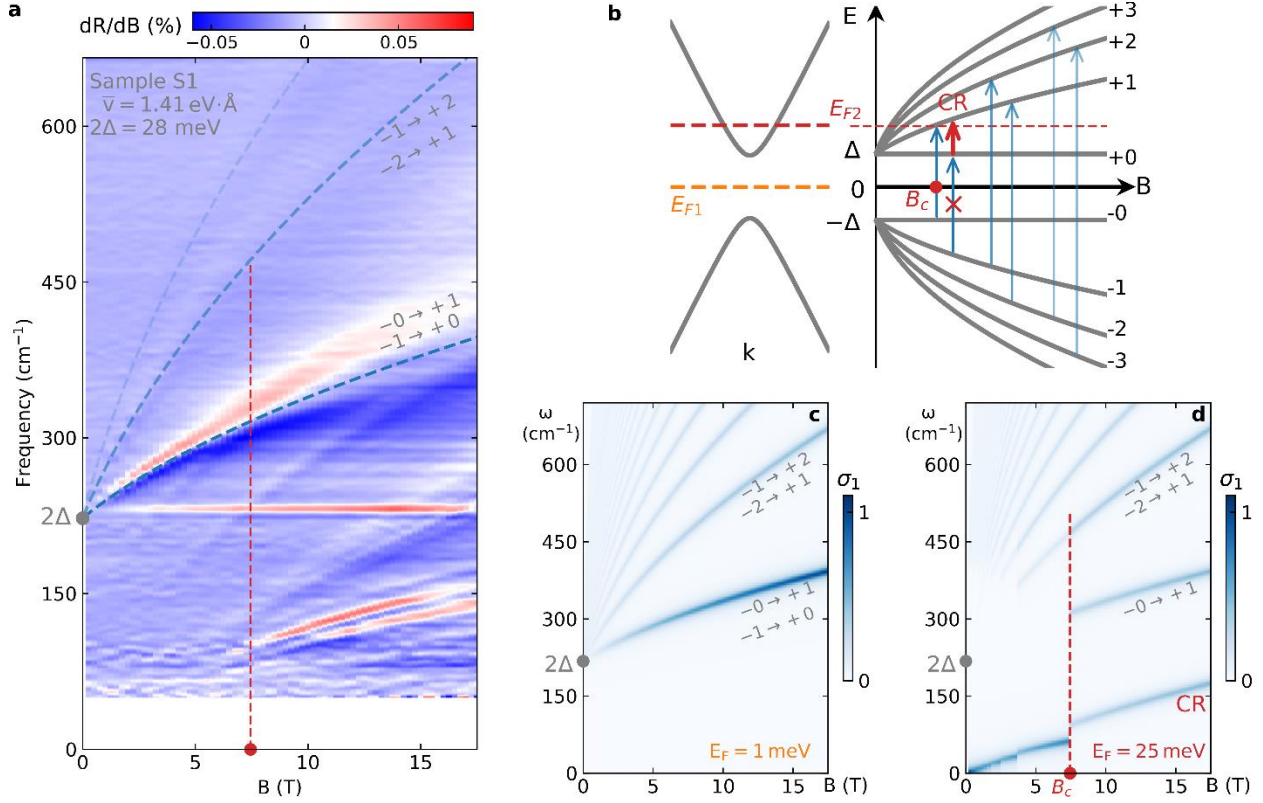
Extended Data Fig. 1|Nodal-line crossing point models. Three different two-band models for the crossing point of two nodal-lines at $\mathbf{k} = (0, 0, 0)$. **a**, Fermi surface (FS) near the crossing of two straight nodal-lines, described by the Hamiltonian²⁰ $H_1 = k_y\tau_x + k_xk_z\tau_z$. **b**, FS near the crossing of two parabolic nodal-lines, described by the Hamiltonian²³ $H_2 = (k_x + k_y^2 - k_z^2)\tau_x + k_yk_z\tau_z$. **c**, FS near the crossing of one straight and one parabolic nodal-line, described by the Hamiltonian $H_3 = tk_z^2\tau_0 + \left(\frac{k_z^2}{2m} + vk_y\right)\tau_z + k_xk_z\tau_x + \Delta\tau_y$, where Δ is half of the spin-orbit coupling (SOC) gap. The band structures at $k_x = 0$ for the three different crossing points are shown in **d**, **e**, and **f** for H_1 , H_2 , and H_3 , respectively. **g**, The FS contour at $k_x = 0$ for H_1 , showing an open orbit for magnetic field $B \parallel k_x$. **h**, The area of the closed orbit $S(E)$ at $k_x = 0$ for H_2 increases linearly with energy. **i**, $S(E)$ increases as $E^{3/2}$ at $k_x = 0$ for H_3 and remains $E^{3/2}$ for energies higher than the SOC gap. Here, $t = 0.3, v = 2, m = 0.5, \Delta = 0.014$.



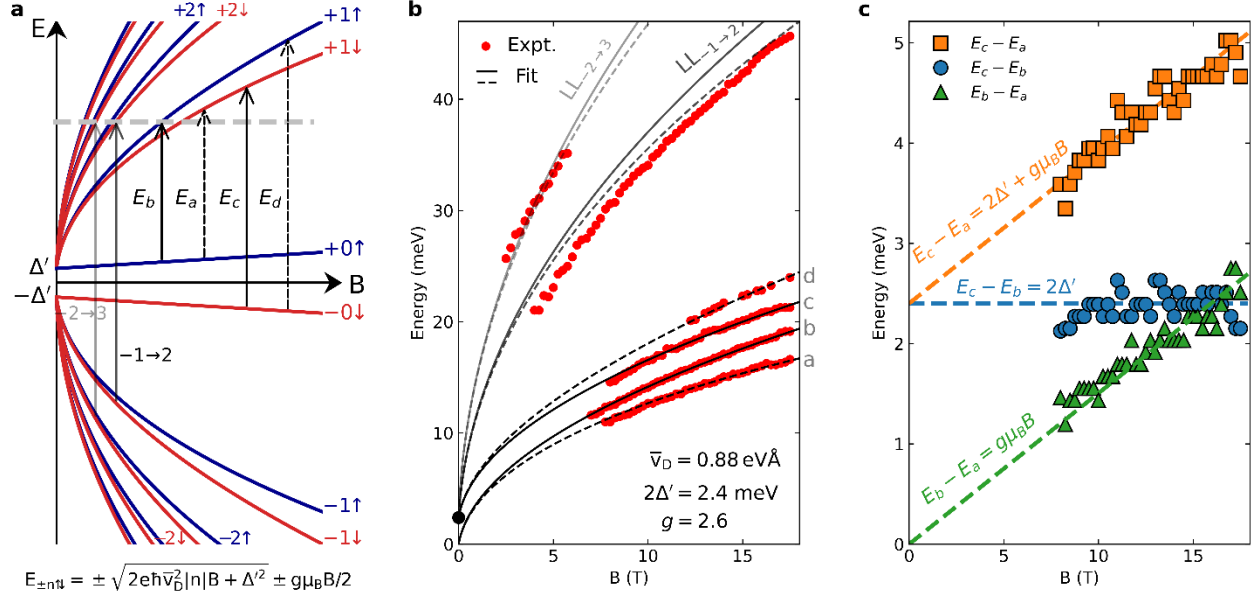
Extended Data Fig. 2|Different power-laws of LL transitions in ZrSiS. a, Second derivative d^2R/dB^2 data colormap for ZrSiS (Sample S2) plotted on log-log scale from 1 T to 17.5 T. **b**, Line guides for LL transitions originated from different fermions. Gray solid lines represent the lowest three interband LL transitions for the gapped Dirac cone. Orange lines indicate the LL transitions associated with Dirac-like fermions, with $E \propto \sqrt{nB}$ or $\frac{\Delta \ln(E)}{\Delta \ln(B)} = \frac{1}{2}$. Purple lines indicate the LL transitions associated with semi-Dirac fermions, with $E \propto B^{2/3}$ or $\frac{\Delta \ln(E)}{\Delta \ln(B)} = \frac{2}{3}$.



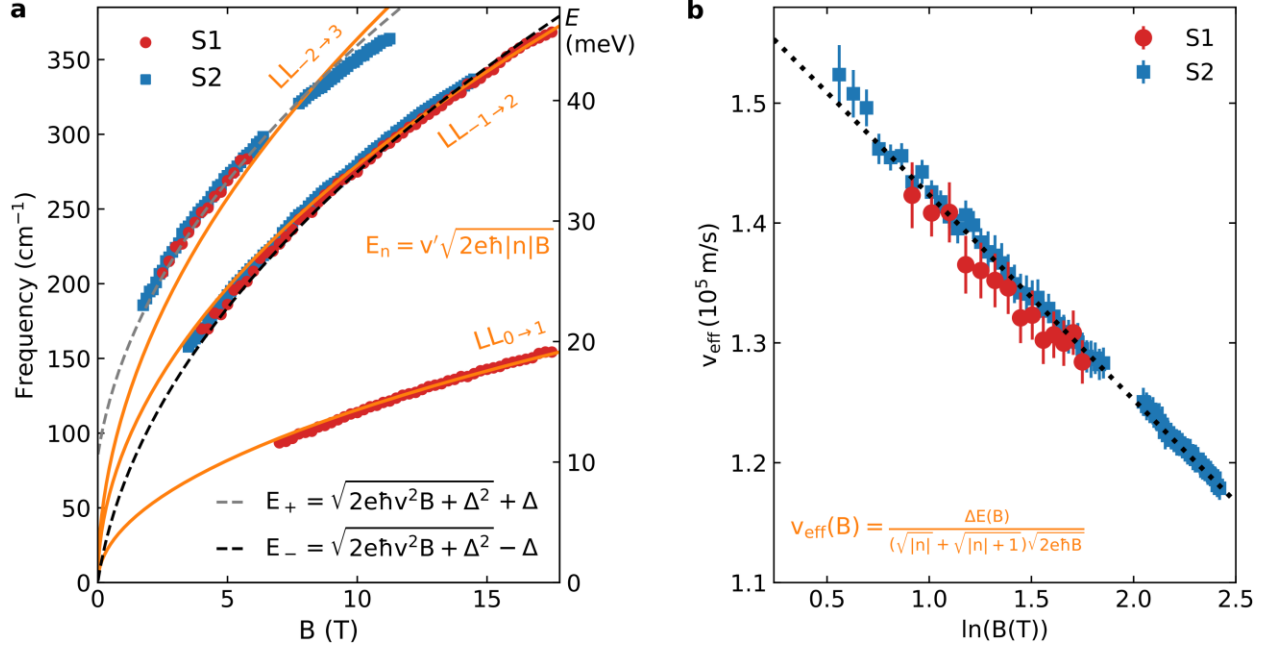
Extended Data Fig. 3|Determination of the LL transition energy. **a**, Second derivative d^2R/dB^2 spectra for ZrSiS (Sample S1) from 7 T to 17.5 T. The spectra are shifted vertically for clarity. Red and purple dots mark the local minima of d^2R/dB^2 that correspond to the LL transitions associated with the Dirac-like and semi-Dirac fermions, respectively. **b**, Second derivative data colormap with LL transition energies overlaid on top as red and purple dots. Black dashed lines are model calculations of the interband LL transitions from the massive Dirac fermion with averaged Fermi velocity $\bar{v} = 1.41 \text{ eV\AA}$ and gap $2\Delta = 28 \text{ meV}$. The gray dashed line marks the predicted dispersion of cyclotron resonance (CR) associated with the massive Dirac fermion if the Fermi level is outside the Dirac gap ($E_{CR} = \sqrt{2e\hbar v^2 B + \Delta^2} - \Delta$). The observed Dirac-like LL transitions (red dots) deviate from the predicted CR behavior associated with the massive Dirac fermion.



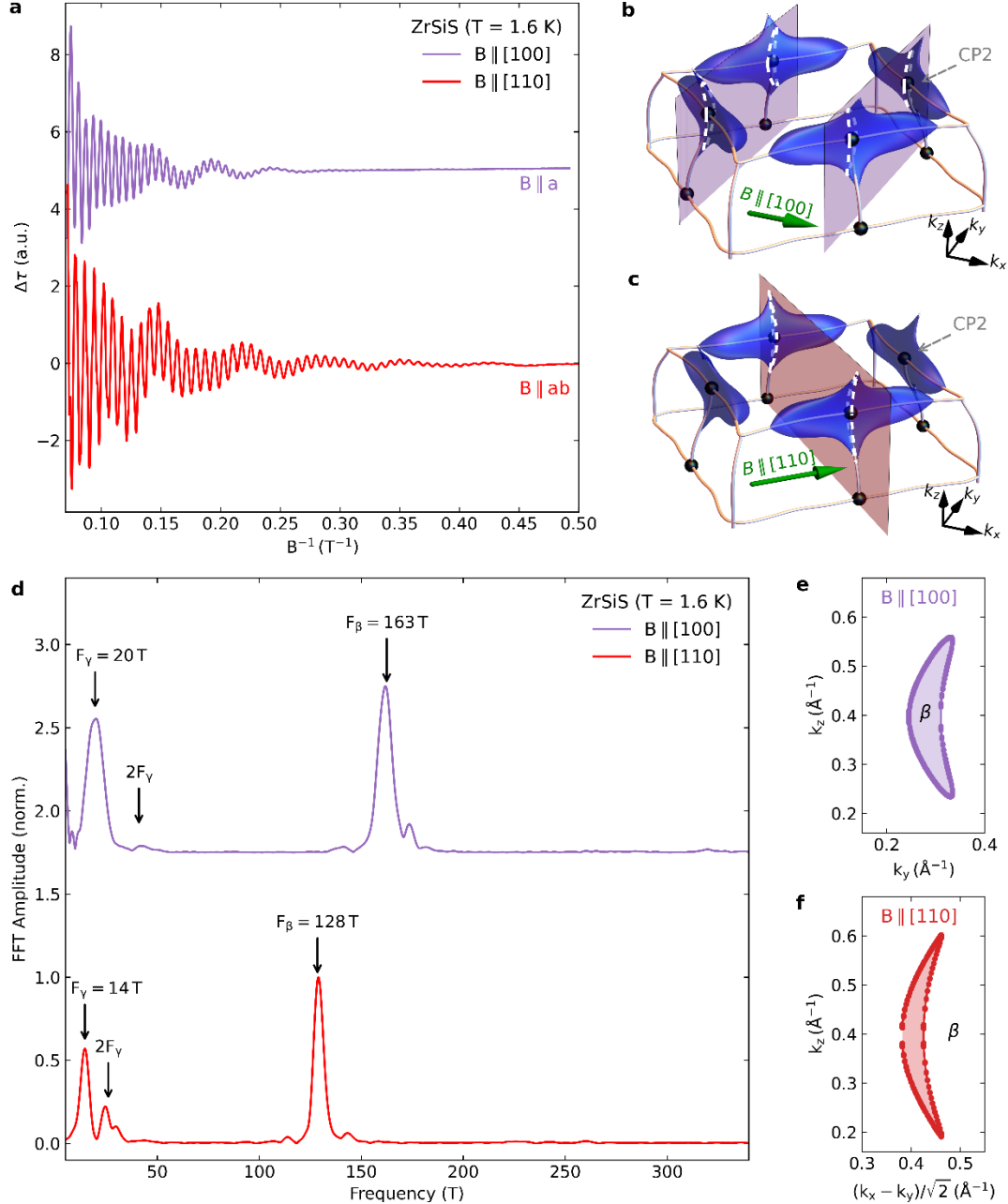
Extended Data Fig. 4|Absence of cyclotron resonance (CR) from the main interband LL transition in ZrSiS. **a**, First derivative dR/dB data for ZrSiS (Sample S1). Blue dashed lines are the model calculations of the main interband LL transitions across the massive Dirac cone (same as in Fig. 2b). The vertical red dashed line marks the critical magnetic field ($B_c \approx 7 \text{ T}$) where the sub-gap transitions onset around 100 cm^{-1} . The $LL_{-0(-1) \rightarrow +1(+0)}$ transition associated with the massive Dirac fermion remain continuous. **b**, Schematic massive Dirac cone (left) and the corresponding LL diagrams (right). When the Fermi energy is inside the Dirac gap (orange dashed line E_{F1}), only interband LL transitions (blue arrows) can happen. If the Fermi energy is outside the Dirac gap (red dashed line E_{F2}), some of the interband LL transitions will be blocked below the critical field B_c (e.g., $LL_{-1 \rightarrow +0}$), and accompanied by the appearance of a lower-energy CR mode (red arrow) above B_c . **c**, **d**, Calculated real part of the optical conductivity σ_1 of a massive Dirac cone ($v_F = 1.41 \text{ eV}\cdot\text{\AA}$ and $2\Delta = 28 \text{ meV}$) with the Fermi energy inside (**c**) and outside (**d**) the gap. Peaks in σ_1 correspond to the series of interband LL transitions. The discontinuity in the $LL_{-0 \rightarrow +1}$ transition (**d**) is inconsistent with the experiment (**a**), indicating that the origin of the sub-gap feature in **a** is not the CR.



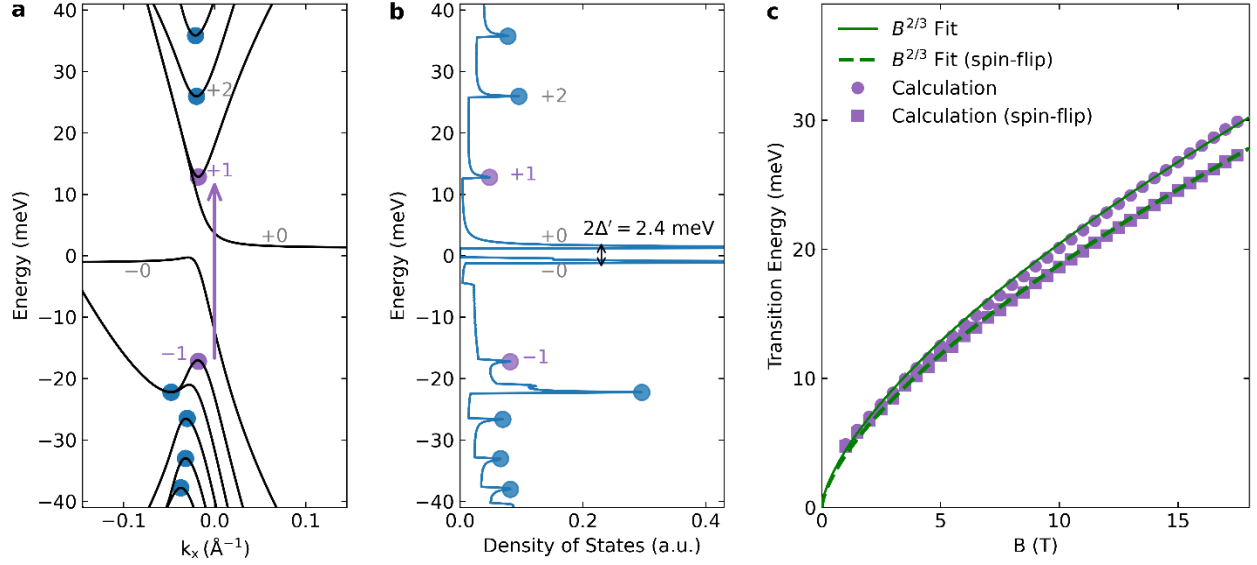
Extended Data Fig. 5 | Landau level diagram and fitting of Dirac-like LL transitions. **a**, LL for the Dirac-like fermion: $E_{\pm n \uparrow \downarrow} = \pm \sqrt{2e\hbar\bar{v}_D^2|n|B + \Delta'^2} \pm g\mu_B B/2$, where n is the LL index, \bar{v}_D is the averaged Fermi velocity, $2\Delta'$ is the SOC gap, and g is the Zeeman g -factor. Blue (red) lines represent the Zeeman-split LLs with up (down) spins. Gray dashed line indicates the Fermi level. Black vertical arrows denote the LL transitions between the 0th and 1st LLs, and the solid (dashed) arrows represent spin-conserving (spin-flip) transitions. Gray vertical arrows denote the $LL_{-1 \rightarrow 2}$ and $LL_{-2 \rightarrow 3}$ transitions. **b**, Fitting of all the Dirac-like LL transitions (red dots) based on the LL diagram in **a** and three parameters \bar{v}_D , $2\Delta'$, and g . Solid and dashed lines represent the spin-conserving and spin-flip transitions, respectively. The four-fold splitting feature (transitions labeled a, b, c, d) is nicely reproduced with $\bar{v}_D = 0.88 \text{ eV\AA}$, $2\Delta' = 2.4 \text{ meV}$, and $g = 2.6$. **c**, Energy differences of the four-fold split-peaks in **b**. $E_b - E_a$ (green triangles) show linear dependence with magnetic field (green dashed line), consistent with the Zeeman-splitting of the final state ($+1 \uparrow$ and $-1 \uparrow$ LL in **a**): $g\mu_B B$. $E_c - E_b$ (blue circles) remain constant with increasing magnetic field and provide a direct measure of the gap size⁵⁰. Since $E_c = E_{+1\downarrow} - E_{-0\downarrow} = \sqrt{2e\hbar\bar{v}_D^2 B + \Delta'^2} + \Delta'$ and $E_b = E_{+1\uparrow} - E_{+0\uparrow} = \sqrt{2e\hbar\bar{v}_D^2 B + \Delta'^2} - \Delta'$, their difference $E_c - E_b = 2\Delta'$. Finally, $E_c - E_a$ (orange squares) also increase linearly with magnetic field (orange dashed line) but have a vertical offset of $2\Delta'$ as $B \rightarrow 0$. This is consistent with the spin-flip transition: $E_a = E_{+1\downarrow} - E_{+0\uparrow} = \sqrt{2e\hbar\bar{v}_D^2 B + \Delta'^2} - \Delta' - g\mu_B B$ and therefore $E_c - E_a = 2\Delta' + g\mu_B B$.



Extended Data Fig. 6|Velocity renormalization and cyclotron resonance interpretations for Dirac-like LL transitions. **a)** The Dirac-like LL transitions for sample S1 and sample S2 are shown as red dots and blue square, respectively. They can be modeled by the $LL_{0 \rightarrow 1}$, $LL_{-1 \rightarrow 2}$, and $LL_{-2 \rightarrow 3}$ transitions (orange lines) associated with a gapless Dirac fermion with $v' = 0.81 \text{ eV\AA}$. Alternatively, the $LL_{-2 \rightarrow 3}$ and $LL_{-1 \rightarrow 2}$ transitions can also be interpreted as the lowest energy interband (E_+) and intraband (E_-) LL transitions of another gapped Dirac fermion, respectively. Gray and black dashed lines correspond to fit with $E_+ = \sqrt{2e\hbar v^2 B + \Delta'^2} + \Delta$ and $E_- = \sqrt{2e\hbar v^2 B + \Delta'^2} - \Delta$, respectively. The fitted gap size is $2\Delta \approx 10.5 \text{ meV}$ and the averaged velocity is $v = 2.24 \text{ eV\AA}$. **b)** Effective velocity v_{eff} obtained from experimental $LL_{-2 \rightarrow 3}$ transition energies⁵⁴ for sample S1 (red dots) and sample S2 (blue squares). The resulting v_{eff} shows a logarithmic dependence on B (black dotted line): a smoking-gun signature for electronic correlations in massless Dirac fermions^{54,55}.



Extended Data Fig. 7|Quantum oscillations in ZrSiS under the in-plane magnetic fields. a, Field dependence of the oscillatory part of the magnetic torque $\Delta\tau$, which exhibits strong quantum oscillations for both $B \parallel [100]$ ($B \parallel a$) and $B \parallel [110]$ ($B \parallel ab$) field orientations. The calculated electron Fermi surface (blue) of ZrSiS is shown with extremal orbits (white dashed lines) for $B \parallel [100]$ in (b) and $B \parallel [110]$ in (c). **d,** Fast Fourier transform (FFT) amplitude of the quantum oscillations in a, showing several oscillation frequencies (F_γ , F_β) and their harmonics, consistent with previous studies⁵⁶. The extremal orbits and k -space area (S) extracted from b and c are shown in e and f for $B \parallel [100]$ and $B \parallel [110]$, respectively. The extremal orbits' areas match with the frequency F_β of the electron pocket near the CP2, according to Onsager's relation $S = 2\pi eF/\hbar$ ($S_{[100]} = 2\pi eF_\beta^{[100]}/\hbar \approx 0.0156 \text{ \AA}^{-2}$, $S_{[110]} = 2\pi eF_\beta^{[110]}/\hbar \approx 0.0121 \text{ \AA}^{-2}$).



Extended Data Fig. 8|Landau level calculation of the crossing nodal-line model. a,

Numerically calculated Landau level (LL) for Eq. (1): $H_{CP} = t_1 k_z^2 \tau_0 + \left(\frac{k_z^2}{2m} + v(k_x - k_y) \right) \tau_z + t_2(k_x + k_y)k_z \tau_x + \Delta' \tau_y$ for $B = 17.5$ T along k_x (see Supplementary Sec. IV). The model parameters are determined from fitting the DFT band structure near CP1 ($t_1 = 0.559 \text{ eV}\text{\AA}^2$, $m = 0.0624 \text{ eV}^{-1}\text{\AA}^{-2}$, $v = 3.904 \text{ eV}\text{\AA}$, $t_2 = 6 \text{ eV}\text{\AA}^2$, see Supplementary Sec. III). We consider a small gap $2\Delta' = 2.4$ meV due to SOC, similar to the Dirac-like transitions (Extended Data Fig. 5). The LLs disperse along the field direction (k_x) and exhibit extremal points marked by blue and purple dots. Purple vertical arrow marks the lowest order optical transition ($LL_{-1 \rightarrow +1}$) that conserves the momentum k_x . Summing over k_x gives a continuum of absorption but with singularities arising from extremal points. **b,** Calculated density of states (DOS) of the 1D-like LL band in **a**. Blue and purple dots mark the peaks in DOS resulting from the singularities in the LL bands. **c,** Calculated energies of the lowest order momentum-conserving optical transition $LL_{-1 \rightarrow +1}$ (purple arrow in **a**) as a function of magnetic field are shown as purple dots. Spin-flip LL transitions assuming a Zeeman g-factor $g = 2.6$ (Extended Data Fig. 5) are shown as purple squares. Green solid (dashed) line are fits of the calculated spin-conserving (spin-flip) transition energies, demonstrating the $B^{2/3}$ scaling behavior in the LLs of the crossing nodal-line model at the semi-Dirac point.

Acknowledgements

Magneto-optical spectroscopy of ZrSiS is supported by NSF-DMR 2210186. Research on the electrodynamics of semi-Dirac quasiparticles, including the theoretical analysis of Landau Levels spectra at Columbia, is supported as part of Programmable Quantum Materials, an Energy Frontier Research Center funded by the U.S. Department of Energy (DOE), Office of Science, Basic Energy Sciences (BES), under award DE-SC0019443. D.N.B. is Moore Investigator in Quantum Materials EPIQS GBMF9455. Support for crystal growth and characterization at Penn State was provided by the National Science Foundation through the Penn State 2D Crystal Consortium-Materials Innovation Platform (2DCC-MIP) under NSF Cooperative Agreement DMR-1539916 and NSF-DMR 2039351. The National High Magnetic Field Laboratory is supported by the National Science Foundation through NSF/DMR-1644779, NSF/DMR-2128556 and the State of Florida. The work of A.N.R. and M.I.K. was supported by the European Union's Horizon 2020 research and innovation program under European Research Council Synergy Grant 854843 "FASTCORR". The work of M.I.K. was further supported by the Dutch Research Council (NWO) via the "TOPCORE" consortium. The Flatiron Institute is a division of the Simons Foundation.

Author Contributions

Y.S. conceived the experimental idea and supervised the project with D.N.B. Y.S. and S.M. performed the high-field magneto-optical measurements with help from M.O. and D.S. D.G. performed the quantum oscillation measurements. Y.S. analyzed the data with help from A.N.R., J.W., Z.S., R.Q., M.I.K., and A.J.M. A.N.R. performed the *ab initio* calculations on ZrSiS and model calculations in magnetic fields were performed by JW and AJM. Y.Z., S.H.L., and Z.Q.M. synthesized the ZrSiS single crystals. Y.S. and D.N.B. wrote the manuscript, with input from all co-authors.

Competing interests

The authors declare no competing interests.

Data Availability

Source data are provided with this paper. All other data that support the findings of this study are available from the corresponding authors upon reasonable request.

Code Availability

The codes used for data analysis are available from the corresponding authors upon reasonable request.

Methods

Single-crystal synthesis and characterization

The ZrSiS single crystals were synthesized using a chemical vapor transport method as described previously¹⁶.

Voigt magneto-optical spectroscopy and the absence of surface states

High-field magneto-optical measurements were performed at $T \approx 5$ K under Voigt geometry ($B \perp c$ and $\parallel a$) at the National High Magnetic Field Laboratory. A Bruker Vertex 80V FTIR spectrometer combined with a 17.5 T superconducting magnet was utilized to record the reflectance spectra of ZrSiS at zero and high magnetic field. Infrared beam from a Globar lamp was focused on the (001) surface of ZrSiS crystal. The typical size of ZrSiS crystals used in our measurements is $\sim 4 \text{ mm} \times 4 \text{ mm} \times 0.3 \text{ mm}$ and the spot size of the infrared beam is smaller than the lateral size of the sample. We remark that there are various surface states^{15,42,57,58} reported in the ZrSiS family of topological semimetals. These surface states are strictly confined to the top and bottom surfaces of ZrSiS and do not contribute to the out-of-plane orbital motion when the magnetic field is applied in-plane. Therefore, we rule out the contribution of surface states at the top and/or side surfaces of the crystal in our magneto-optical data.

Density functional theory calculation

DFT calculations were carried out using the plane-wave pseudopotential method as implemented in the Quantum ESPRESSO simulation package^{59,60}. Norm-conserving pseudopotentials⁶¹ were used in conjunction with the local density approximation for exchange-correlation potential. An energy cutoff of 70 Ry for the plane-waves and a convergence threshold of 10^{-12} Ry were used for the self-consistent solution of the Kohn-Sham equations. The Brillouin zone was sampled by a $14 \times 14 \times 6$ Monkhorst-Pack⁶² k-point mesh. Lattice constants were relaxed, resulting in $a = 3.4665 \text{ \AA}$ and $c = 7.9148 \text{ \AA}$. The atomic structure within the unit cell was relaxed until the residual forces were less than 10^{-4} Ry/bohr.

To ensure the numerical accuracy of the Fermi surface calculations and related properties, an interpolation scheme based on the maximally localized Wannier functions (MLWF)⁶³ was used. For this purpose, we used the wannier90 code⁶⁴ to construct an extended tight-binding Hamiltonian for ZrSiS in the MLWF basis, which included the 3s and 3p states for Si and S as well as the 4s and 4d states for Zr. The interpolated band energies ensure a correct description of the DFT band structure within the range of at least ± 10 eV relative to the Fermi energy.

Quantum oscillations in ZrSiS with torque magnetometry measurements

The torque magnetometry measurements up to 14 T were performed using a piezoresistive cantilever in a superconducting magnet equipped with a variable temperature insert (VTI). A single crystal of ZrSiS is fixed to the end of a 0.30 mm cantilever arm with vacuum grease. A jet of Helium-4 gas from the inlet of the VTI onto the cryostat kept the samples at a constant temperature of 1.6 K during the measurements. There are two resistive elements on the cantilever, one of which is located at the base of the arm and experiences strain with a change in the sample magnetization. The second resistive element is not affected by the torque but mimics the temperature and magnetic field dependence of the first. These are combined with two more

resistors at room temperature to form a Wheatstone bridge that can be balanced at low temperatures before changing the magnetic field. A small current is applied across the bridge circuit and the measured voltage records the changing torque τ created by the de Haas-van Alphen (dHvA) effect.

Semi-Dirac fermions in the nodal-ring model

To illustrate the semi-Dirac fermions in the nodal-ring model, we consider the nodal-ring Hamiltonian^{65,66}: $H_R(\mathbf{k}) = (k_x^2 + k_y^2 - k_0^2)\tau_x + vk_z\tau_z$, where v is the Fermi velocity along z , τ_0 is the identity matrix, and τ_x, τ_z are the Pauli matrices for orbitals. The corresponding energy spectrum is:

$$E_R(\mathbf{k}) = \pm \sqrt{(k_x^2 + k_y^2 - k_0^2)^2 + v^2 k_z^2} \quad (2)$$

and a Dirac nodal-ring at $k_z = 0$ with radius $k_0 = \sqrt{k_x^2 + k_y^2}$ can be identified. This nodal-ring marks a protected crossing of two bands along a ring in momentum space and at any point on the ring the spectrum is Dirac. Remarkably, at $k_x = \pm k_0$, the projection of constant energy contours onto the $k_y - k_z$ plane yields contours of the semi-Dirac form^{6,66} $E_{SD} = \pm \sqrt{k_y^4/4m^2 + v^2 k_z^2}$ that describes a massive fermion along k_y ($m = 0.5$) and massless Dirac fermion along k_z (see Supplementary Video 1). Under the in-plane magnetic field, the area of the cyclotron orbit at energy E is $S(E) \propto E^{3/2} \sqrt{m}/v$, which leads to the $B^{2/3}$ scaling of LLs^{3,66}. Here, we briefly describe the solution of the Hamiltonian in an in-plane magnetic field \mathbf{B} directed along x that reveals the main features of the absorption spectrum. Choosing the Landau gauge $\mathbf{A} = (0, Bz, 0)$ and rescaling the coordinate $z \rightarrow l_B u$ with magnetic length $l_B = \frac{k_0}{\sqrt{B}}$ and defining field scale $B_0 = k_0^2$ and rescaled field $b = \frac{B}{B_0}$, we have $H_R(\mathbf{k}) = \frac{1}{l_B} (V(u)\tau_x - i\partial_u \partial \tau_z)$ with $V(u) = \frac{1}{\sqrt{b}} (- (1 - \frac{k_x^2}{k_0^2}) + bu^2)$. From this form of V one can see that for $(1 - \frac{k_x^2}{k_0^2}) \neq 0$, V is minimized at a particular u^2 expanding around the two u values that give Dirac spectra, while when $k_x^2 = k_0^2$ we have a semi-Dirac equation. We have solved the corresponding Schrödinger equation numerically by observing that at each k_x , H_R^2 can be diagonalized trivially yielding two second order differential equations that we solve by discretization. The current operator can then be obtained as a differential operator and applied to the solutions. Integration of the resulting absorption spectrum over k_x gives the continuum absorptions, with singularities at the upper edge scaling as $B^{1/2}$ and lower edge as $B^{2/3}$, consistent with previous results⁶⁶. While the nodal-ring model is not directly relevant to the interpretation of our experimental results, it does display the generic features of an absorption continuum with upper and lower edges scaling differently with B , and with the characteristic Dirac and semi-Dirac behaviors.

Semiclassical quantization of the crossing nodal-line model

To obtain the Landau level scaling of the semi-Dirac fermion at the CP of nodal-lines, we consider the following Hamiltonian: $H_3 = tk_z^2\tau_0 + \left(\frac{k_z^2}{2m} - vk_y\right)\tau_z + k_x k_z \tau_x$, which has an

extremal Fermi surface at $k_x = 0$ for $B \parallel k_x$. This model also describes the crossing of one straight and one curved nodal-line and is related to the model Eq. (1) by a 45-degree in-plane rotation. The corresponding eigenvalue $E_3 = tk_z^2 \pm \sqrt{k_z^4/4m^2 - vk_z^2k_y/m + v^2k_y^2 + k_x^2k_z^2}$.

For a magnetic field B applied along k_x , the eigenvalue spectrum has extremal values at $k_x = 0$. Without loss of generality, we consider the Fermi surface of the electron pockets ($m > 0$) and choose $v > 0$, $E > 0$, and $0 < t < (2m)^{-1}$. The cross-section of the electron Fermi surface (FS) at constant energy E is then determined by:

$$E = tk_z^2 \pm \left(\frac{k_z^2}{2m} - vk_y \right) \quad (3)$$

, which is bounded by two parabolic curves: $k_y^+ = \frac{E}{v} - \left(t - \frac{1}{2m} \right) k_z^2/v$ and $k_y^- = -\frac{E}{v} + \left(t + \frac{1}{2m} \right) k_z^2/v$. These two parabolic curves intersect at $k_z^2 = E/t \equiv a^2$, forming a crescent-shaped closed contour for electron orbits (see inset of Extended Data Fig. 1i). If $k_z^2 > E/t$, the hole FS is obtained with $E = tk_z^2 - \left(\frac{k_z^2}{2m} - vk_y \right)$. The area of the electron FS contour can be obtained by evaluating the difference between the areas of the parabolic segments of k_y^- and k_y^+ :

$$S(E) = S^-(E) - S^+(E) = \int_{-a}^a (k_y^+ - k_y^-) dk_z = \int_{-a}^a \frac{2E}{v} \left(1 - \frac{k_z^2}{a^2} \right) dk_z = \frac{8}{3} \frac{E^{\frac{3}{2}}}{\sqrt{tv}} \quad (4)$$

Following Onsager's quantization relation $S(E) = 2\pi(n + \gamma)eB/\hbar$ where n is the Landau level index and γ is the phase factor, we obtain the $B^{2/3}$ scaling of LLs: $E_n \propto (n + \gamma)^{2/3} B^{2/3}$.

In the presence of finite SOC, the degeneracy at the semi-Dirac point is lifted but the characteristic band dispersions and LL scaling recover at energies higher than the SOC gap. We illustrate the case with SOC using the following Hamiltonian:

$$H'_3 = H_3 + \Delta\tau_y = tk_z^2\tau_0 + \left(\frac{k_z^2}{2m} - vk_y \right) \tau_z + k_x k_z \tau_x + \Delta\tau_y, \quad (5)$$

where 2Δ is the size of the SOC gap.

The area of the electron FS contour with SOC becomes:

$$S_{SOC}(E) = \frac{8}{3} \frac{\sqrt{E + \Delta}}{\sqrt{tv}} \left(e_E \left[1 - \frac{2\Delta}{E + \Delta} \right] E - e_K \left[1 - \frac{2\Delta}{E + \Delta} \right] \Delta \right), \quad (6)$$

where $e_E[x]$ and $e_K[x]$ denotes the complete elliptic integral of the second kind and first kind, respectively. Eq. (6) can be solved numerically and the resulting $S_{SOC}(E)$ is shown in Extended Data Fig. 1i, where the $S_{SOC}(E) \propto E^{3/2}$ behavior is recovered at energies higher than around 2Δ .

Different crossing points in ZrSiS

As shown in Fig. 1c the near Fermi surface electronic structure of ZrSiS arises from nodal squares in the $k_x - k_y$ plane intersecting with curved nodal lines running along k_z . There are

two generic types of crossing points in ZrSiS: at the corners of the nodal squares (deep inside the hole Fermi surface in Fig. 1c) and at the midpoint of the edge of the nodal squares (CP1 and CP2, black dots in Fig. 1c, Fig. 3b inset). At the former “corner” crossing points, examination of the DFT bands shows that the dispersion becomes quadratic in both directions (similar to Extended Data Fig. 1b, 1c), leading to a conventional B-linear LL spectrum. However, at the crossing point labelled CP1 and CP2, only the z-direction dispersion becomes quadratic: the in-plane dispersion remains linear so that the Hamiltonian in the vicinity of a crossing point may be written as Eq. (1).

References

1. Armitage, N. P., Mele, E. J. & Vishwanath, A. Weyl and Dirac semimetals in three-dimensional solids. *Rev. Mod. Phys.* **90**, 015001 (2018).
2. Lv, B. Q., Qian, T. & Ding, H. Experimental perspective on three-dimensional topological semimetals. *Rev. Mod. Phys.* **93**, 025002 (2021).
3. Dietl, P., Piéchon, F. & Montambaux, G. New Magnetic Field Dependence of Landau Levels in a Graphenelike Structure. *Phys. Rev. Lett.* **100**, 236405 (2008).
4. Pardo, V. & Pickett, W. E. Half-Metallic Semi-Dirac-Point Generated by Quantum Confinement in TiO_2/VO_2 Nanostructures. *Phys. Rev. Lett.* **102**, 166803 (2009).
5. Banerjee, S., Singh, R. R. P., Pardo, V. & Pickett, W. E. Tight-Binding Modeling and Low-Energy Behavior of the Semi-Dirac Point. *Phys. Rev. Lett.* **103**, 016402 (2009).
6. Montambaux, G., Piéchon, F., Fuchs, J.-N. & Goerbig, M. O. Merging of Dirac points in a two-dimensional crystal. *Phys. Rev. B* **80**, 153412 (2009).
7. Delplace, P. & Montambaux, G. Semi-Dirac point in the Hofstadter spectrum. *Phys. Rev. B* **82**, 035438 (2010).
8. Dóra, B., Herbut, I. F. & Moessner, R. Coupling, merging, and splitting Dirac points by electron-electron interaction. *Phys. Rev. B* **88**, 075126 (2013).

9. Huang, H., Liu, Z., Zhang, H., Duan, W. & Vanderbilt, D. Emergence of a Chern-insulating state from a semi-Dirac dispersion. *Phys. Rev. B* **92**, 161115 (2015).
10. Saha, K. Photoinduced Chern insulating states in semi-Dirac materials. *Phys. Rev. B* **94**, 081103 (2016).
11. Roy, B. & Foster, M. S. Quantum Multicriticality near the Dirac-Semimetal to Band-Insulator Critical Point in Two Dimensions: A Controlled Ascent from One Dimension. *Phys. Rev. X* **8**, 011049 (2018).
12. Uryszek, M. D., Christou, E., Jaefari, A., Krüger, F. & Uchoa, B. Quantum criticality of semi-Dirac fermions in $2+1$ dimensions. *Phys. Rev. B* **100**, 155101 (2019).
13. Kotov, V. N., Uchoa, B. & Sushkov, O. P. Coulomb interactions and renormalization of semi-Dirac fermions near a topological Lifshitz transition. *Phys. Rev. B* **103**, 045403 (2021).
14. Mohanta, N. *et al.* Semi-Dirac and Weyl fermions in transition metal oxides. *Phys. Rev. B* **104**, 235121 (2021).
15. Schoop, L. M. *et al.* Dirac cone protected by non-symmorphic symmetry and three-dimensional Dirac line node in ZrSiS. *Nat. Commun.* **7**, 11696 (2016).
16. Hu, J. *et al.* Evidence of Topological Nodal-Line Fermions in ZrSiSe and ZrSiTe. *Phys. Rev. Lett.* **117**, 016602 (2016).
17. Kim, Y., Wieder, B. J., Kane, C. L. & Rappe, A. M. Dirac Line Nodes in Inversion-Symmetric Crystals. *Phys. Rev. Lett.* **115**, 036806 (2015).
18. Fang, C., Chen, Y., Kee, H.-Y. & Fu, L. Topological nodal line semimetals with and without spin-orbital coupling. *Phys. Rev. B* **92**, 081201 (2015).
19. Bzdušek, T., Wu, Q., Rüegg, A., Sigrist, M. & Soluyanov, A. A. Nodal-chain metals. *Nature* **538**, 75–78 (2016).
20. Yan, Q. *et al.* Experimental discovery of nodal chains. *Nat. Phys.* **14**, 461–464 (2018).

21. Chang, G. *et al.* Topological Hopf and Chain Link Semimetal States and Their Application to Co_2MnGa . *Phys. Rev. Lett.* **119**, 156401 (2017).
22. Chen, W., Lu, H.-Z. & Hou, J.-M. Topological semimetals with a double-helix nodal link. *Phys. Rev. B* **96**, 041102 (2017).
23. Wu, Q., Soluyanov, A. A. & Bzdušek, T. Non-Abelian band topology in noninteracting metals. *Science* **365**, 1273–1277 (2019).
24. Novoselov, K. S. *et al.* Two-dimensional gas of massless Dirac fermions in graphene. *Nature* **438**, 197–200 (2005).
25. Zhang, Y., Tan, Y.-W., Stormer, H. L. & Kim, P. Experimental observation of the quantum Hall effect and Berry's phase in graphene. *Nature* **438**, 201–204 (2005).
26. Katsnelson, M. I., Novoselov, K. S. & Geim, A. K. Chiral tunnelling and the Klein paradox in graphene. *Nat. Phys.* **2**, 620–625 (2006).
27. Young, A. F. & Kim, P. Quantum interference and Klein tunnelling in graphene heterojunctions. *Nat. Phys.* **5**, 222–226 (2009).
28. Sadowski, M. L., Martinez, G., Potemski, M., Berger, C. & de Heer, W. A. Landau Level Spectroscopy of Ultrathin Graphite Layers. *Phys. Rev. Lett.* **97**, 266405 (2006).
29. Jiang, Z. *et al.* Infrared Spectroscopy of Landau Levels of Graphene. *Phys. Rev. Lett.* **98**, 197403 (2007).
30. Orlita, M. *et al.* Approaching the Dirac Point in High-Mobility Multilayer Epitaxial Graphene. *Phys. Rev. Lett.* **101**, 267601 (2008).
31. Goerbig, M. O., Fuchs, J.-N., Montambaux, G. & Piéchon, F. Tilted anisotropic Dirac cones in quinoid-type graphene and α -(BEDT-TTF) $_2\text{I}_3$. *Phys. Rev. B* **78**, 045415 (2008).
32. Pereira, V. M., Castro Neto, A. H. & Peres, N. M. R. Tight-binding approach to uniaxial strain in graphene. *Phys. Rev. B* **80**, 045401 (2009).

33. Kim, J. *et al.* Observation of tunable band gap and anisotropic Dirac semimetal state in black phosphorus. *Science* **349**, 723–726 (2015).
34. Kim, J. *et al.* Two-Dimensional Dirac Fermions Protected by Space-Time Inversion Symmetry in Black Phosphorus. *Phys. Rev. Lett.* **119**, 226801 (2017).
35. Rudenko, A. N., Yuan, S. & Katsnelson, M. I. Toward a realistic description of multilayer black phosphorus: From $\$GW\$$ approximation to large-scale tight-binding simulations. *Phys. Rev. B* **92**, 085419 (2015).
36. Tarruell, L., Greif, D., Uehlinger, T., Jotzu, G. & Esslinger, T. Creating, moving and merging Dirac points with a Fermi gas in a tunable honeycomb lattice. *Nature* **483**, 302–305 (2012).
37. Bellec, M., Kuhl, U., Montambaux, G. & Mortessagne, F. Topological Transition of Dirac Points in a Microwave Experiment. *Phys. Rev. Lett.* **110**, 033902 (2013).
38. Rechtsman, M. C. *et al.* Topological Creation and Destruction of Edge States in Photonic Graphene. *Phys. Rev. Lett.* **111**, 103901 (2013).
39. Real, B. *et al.* Semi-Dirac Transport and Anisotropic Localization in Polariton Honeycomb Lattices. *Phys. Rev. Lett.* **125**, 186601 (2020).
40. Isobe, H., Yang, B.-J., Chubukov, A., Schmalian, J. & Nagaosa, N. Emergent Non-Fermi-Liquid at the Quantum Critical Point of a Topological Phase Transition in Two Dimensions. *Phys. Rev. Lett.* **116**, 076803 (2016).
41. Onsager, L. Interpretation of the de Haas-van Alphen effect. *The London, Edinburgh, and Dublin Philosophical Magazine and Journal of Science* **43**, 1006–1008 (1952).
42. Muechler, L. *et al.* Modular Arithmetic with Nodal Lines: Drumhead Surface States in ZrSiTe. *Phys. Rev. X* **10**, 011026 (2020).
43. Schilling, M. B., Schoop, L. M., Lotsch, B. V., Dressel, M. & Pronin, A. V. Flat Optical Conductivity in ZrSiS due to Two-Dimensional Dirac Bands. *Phys. Rev. Lett.* **119**, 187401 (2017).

44. Rudenko, A. N., Stepanov, E. A., Lichtenstein, A. I. & Katsnelson, M. I. Excitonic Instability and Pseudogap Formation in Nodal Line Semimetal ZrSiS. *Phys. Rev. Lett.* **120**, 216401 (2018).
45. Shao, Y. *et al.* Electronic correlations in nodal-line semimetals. *Nat. Phys.* **16**, 636–641 (2020).
46. Shao, Y. *et al.* Optical signatures of Dirac nodal lines in NbAs₂. *Proc. Natl. Acad. Sci. U. S. A.* **116**, 1168–1173 (2019).
47. Santos-Cottin, D. *et al.* Optical conductivity signatures of open Dirac nodal lines. *Phys. Rev. B* **104**, L201115 (2021).
48. Wyzula, J. *et al.* Lorentz-Boost-Driven Magneto-Optics in a Dirac Nodal-Line Semimetal. *Adv. Sci.* **9**, 2105720 (2022).
49. Uykur, E. *et al.* Magneto-optical probe of the fully gapped Dirac band in ZrSiS. *Phys. Rev. Research* **1**, 032015 (2019).
50. Mohelsky, I. *et al.* Temperature dependence of the energy band gap in ZrTe₅: Implications for the topological phase. *Phys. Rev. B* **107**, L041202 (2023).
51. Chen, R. Y. *et al.* Magnetoinfrared Spectroscopy of Landau Levels and Zeeman Splitting of Three-Dimensional Massless Dirac Fermions in ZrTe₅. *Phys. Rev. Lett.* **115**, 176404 (2015).
52. Pack, J. *et al.* Broken Symmetries and Kohn’s Theorem in Graphene Cyclotron Resonance. *Phys. Rev. X* **10**, 041006 (2020).
53. Cao, Y. *et al.* Correlated insulator behaviour at half-filling in magic-angle graphene superlattices. *Nature* **556**, 80–84 (2018).
54. Faugeras, C. *et al.* Landau Level Spectroscopy of Electron-Electron Interactions in Graphene. *Phys. Rev. Lett.* **114**, 126804 (2015).
55. Nedoliuk, I. O., Hu, S., Geim, A. K. & Kuzmenko, A. B. Colossal infrared and terahertz magneto-optical activity in a two-dimensional Dirac material. *Nat. Nano.* **14**, 756–761 (2019).

56. Yang, Y. *et al.* Anisotropic Berry phase in the Dirac nodal-line semimetal ZrSiS: The effect of spin-orbit coupling. *Phys. Rev. B* **103**, 125160 (2021).
57. Topp, A. *et al.* Surface Floating 2D Bands in Layered Nonsymmorphic Semimetals: ZrSiS and Related Compounds. *Phys. Rev. X* **7**, 041073 (2017).
58. Nakamura, T. *et al.* Evidence for bulk nodal loops and universality of Dirac-node arc surface states in ZrGeX_c (X_c = S, Se, Te). *Phys. Rev. B* **99**, 245105 (2019).
59. Giannozzi, P. *et al.* QUANTUM ESPRESSO: a modular and open-source software project for quantum simulations of materials. *J. Phys.: Condens. Matter* **21**, 395502 (2009).
60. Giannozzi, P. *et al.* Advanced capabilities for materials modelling with Quantum ESPRESSO. *J. Phys.: Condens. Matter* **29**, 465901 (2017).
61. Prandini, G., Marrazzo, A., Castelli, I. E., Mounet, N. & Marzari, N. Precision and efficiency in solid-state pseudopotential calculations. *npj Computation Materials* **4**, 72 (2018).
62. Monkhorst, H. J. & Pack, J. D. Special points for Brillouin-zone integrations. *Phys. Rev. B* **13**, 5188–5192 (1976).
63. Marzari, N., Mostofi, A. A., Yates, J. R., Souza, I. & Vanderbilt, D. Maximally localized Wannier functions: Theory and applications. *Rev. Mod. Phys.* **84**, 1419–1475 (2012).
64. Mostofi, A. A. *et al.* An updated version of wannier90: A tool for obtaining maximally-localised Wannier functions. *Comput. Phys. Commun.* **185**, 2309–2310 (2014).
65. Yang, H., Moessner, R. & Lim, L.-K. Quantum oscillations in nodal line systems. *Phys. Rev. B* **97**, 165118 (2018).
66. Oroszlány, L., Dóra, B., Cserti, J. & Cortijo, A. Topological and trivial magnetic oscillations in nodal loop semimetals. *Phys. Rev. B* **97**, 205107 (2018).